

Cite this: *J. Mater. Chem. A*, 2017, 5, 9775

CNT-threaded N-doped porous carbon film as binder-free electrode for high-capacity supercapacitor and Li–S battery†

Yazhi Liu,^{‡a} Gaoran Li,^{‡b} Zhongwei Chen^b and Xinsheng Peng^{*,a}

A novel lightweight, free-standing, CNT-threaded nitrogen-doped porous carbon film (CNCF) has been synthesized as a binder-free electrode for supercapacitor and Li–S battery. The meticulous structural design of using CNT to thread the ZIF-8-derived porous carbon polyhedrons together endows the porous carbon thin film with nice flexibility, high surface area ($645.2 \text{ m}^2 \text{ g}^{-1}$), and hierarchical pore structure as well as good nitrogen doping (2.8 at%) and overall electrical conductivity. When used as binder-free electrode for a supercapacitor, the CNCF delivers a high specific capacitance of 340 F g^{-1} at 2 A g^{-1} , long-term stability with a coulombic efficiency of 97.7% after 10 000 cycles at 20 A g^{-1} , and high energy density of 21.1 W h kg^{-1} with a power density of 5000 W kg^{-1} . It can also serve as an efficient sulfur host for the Li–S battery. The S@CNCF electrode exhibits a high discharge capacity of 926 mA h g^{-1} after 200 cycles at 1C, and 614 mA h g^{-1} after 1800 cycles with an ultra-low overall capacity decay of 0.02%/cycle with sulfur loading of 3 mg cm^{-2} . Moreover, when the sulfur loading is increased to 6.9 mg cm^{-2} , the electrode shows a high initial areal capacity of 7.3 mA h cm^{-2} and a volumetric capacity of 0.94 A h cm^{-3} . This film holds promising potential for flexible or film-like high-energy storage systems.

Received 19th February 2017
Accepted 18th April 2017

DOI: 10.1039/c7ta01526g

rsc.li/materials-a

1. Introduction

The blooming development of portable electronic devices has stimulated intensive research on efficient and lightweight energy storage devices.^{1–6} Among various energy storage devices, the supercapacitor and lithium–sulfur battery are recognized as two promising energy suppliers, with the supercapacitor providing high power and the Li–S battery exhibiting high energy density.^{7–11}

Activated carbon has been extensively used as electrode material for supercapacitors and Li–S batteries due to its large BET specific surface area (S_{BET}), chemical stability and low cost.^{12–16} Recently, considerable efforts have been focused on increasing the S_{BET} of activated carbon to improve its specific capacitance. Nevertheless, the internal surface area is not entirely accessible to ions, not to mention the broken electron conductive pathways caused by the post-activation treatment (e.g. KOH activation), which leads to unsatisfactory specific capacitance.^{17,18} Besides, most of the activated carbon materials

require the use of nonconductive polymer binder and black carbon to fabricate the working electrode, which unavoidably increases the inner resistance and introduces unnecessary weight.^{19,20} All of these disadvantages prevent the activated carbon from fulfilling the requirements of high-performance, efficient, and lightweight devices.

By contrast, mechanically robust, binder-free carbon material with large S_{BET} and high electrical conductivity shows great potential to solve the aforementioned problems.^{21–29} Recently, metal–organic frameworks (MOF) have been intensively explored as carbon precursors to prepare porous carbon materials due to their large surface area and regular pore structures.^{30–32} Especially, as a subclass of MOF, zeolitic imidazolate frameworks, such as ZIF-8, have attracted much more attention due to their intrinsic N abundancy, which can increase the electrical conductivity and wettability of the carbon materials.^{33–37} However, similar to activated carbon, the fabrication of ZIF-derived carbon electrode requires additives, significantly limiting the utilization of their surface area and leading to poor rate performance and cycling stability. On the basis of these concerns, carbon nanotubes (CNT), possessing exceptional long-range conductivity with unique one-dimensional structure, are deservedly considered as the most competitive candidate to overcome the drawbacks of powder carbon materials.^{38–40}

Here, we develop an effective method to prepare CNT-threaded ZIF-8 polyhedrons derived free-standing N-doped

^aState Key Laboratory of Silicon Materials, School of Material Science and Engineering, Zhejiang University, Hangzhou 310027, P. R. China. E-mail: pengxinsheng@zju.edu.cn

^bDepartment of Chemical Engineering, University of Waterloo, 200 University Avenue West, Waterloo, Ontario, N2L 3G1, Canada

† Electronic supplementary information (ESI) available. See DOI: 10.1039/c7ta01526g

‡ These authors contribute equally to this work.

porous carbon film (CNCF) through a simple vacuum filtration, *in situ* reaction and subsequent pyrolysis. Benefiting from its interconnected conductive network and CNT penetration in between porous carbon polyhedrons to form a lamellate structure, the as-prepared CNCF exhibits high S_{BET} ($645.2 \text{ m}^2 \text{ g}^{-1}$), hierarchical pore structure and abundant nitrogen doping. The CNCF delivers high specific capacitance (340 F g^{-1} at 2 A g^{-1}) and high energy density (21.1 W h kg^{-1} at a power density of 5000 W kg^{-1}) when used as electrode for aqueous electrolyte supercapacitor. More remarkably, the sulfur-loaded CNCF (S@CNCF) exhibits extraordinary cycling stability when utilized as cathode for the Li-S battery, *i.e.*, with extremely small capacity decay of 0.02% /cycle over 1800 cycles at a high rate of 1C with a sulfur loading of 3 mg cm^{-2} . Simultaneously, the S@CNCF shows high initial areal and volumetric capacity of 7.3 mA h cm^{-2} and 0.94 A h cm^{-3} , respectively, at a high sulfur loading of 6.9 mg cm^{-2} .

2. Experimental section

2.1 Preparation of ZIF-8/CNT hybrid thin film

Before the synthesis of ZIF-8/CNT hybrid thin film, the negatively charged oxidized CNTs were prepared by chemical oxidation in 6 M HNO_3 for 12 h and then dispersed in water by sonication.⁴¹ The positively charged zinc hydroxide nanostrands (ZHN) were prepared by mixing 1.6 mM aminoethanol aqueous solution with 4 mM zinc nitrate aqueous solution under stirring, followed by aging at room temperature for 30 min. Then, a certain amount of CNT solution was added into the ZHN solution under vigorous stirring to form a homogeneous suspension. Next, the suspension was filtered onto a porous polycarbonate (PC) substrate with a pore size of 200 nm , and after peeling off the substrate, a free-standing ZHN/CNT thin film was obtained. The ZIF-8/CNT thin film was obtained after immersing the ZHN/CNT hybrid thin film in 25 mM 2-methylimidazole (2-mIm) ethanol-water (vol : vol = 2 : 3) solution for 24 h. In this work, by simply controlling the volume ratio of ZHN to CNT, ZIF-8/CNT thin films with different weight ratios of 5 : 1, 10 : 1 and 15 : 1 were fabricated, denoted as ZIF-8/CNT-5/1, 10/1 and 15/1, respectively.

2.2 Preparation of free-standing CNCF

The conversion of ZIF-8/CNT thin film into flexible CNCF was achieved through a two-step thermal conversion process. Typically, the ZIF-8/CNT thin film was heated at $80 \text{ }^\circ\text{C}$ under nitrogen gas for 1 h and then pyrolyzed at $900 \text{ }^\circ\text{C}$ for 3 h with a heating rate of $5 \text{ }^\circ\text{C min}^{-1}$. Subsequently, the black product was immersed in diluted HCl aqueous solution to remove zinc-related inorganic nanoparticles resulting from the pyrolysis of ZIF-8 precursor, and then washed with abundant water to obtain the CNCF. Here, three CNCF thin films with weight ratios (ZIF-8/CNT) of 5/1, 10/1 and 15/1 were fabricated under the same conditions and designated as CNCF-5/1, 10/1 and 15/1, respectively. Meanwhile, the pyrolysis product of ZIF-8/CNT-10/1 without acid treatment was named CNCF-10/1@Zn. For comparison, the performance of pure ZIF-8 powder pyrolyzed

under the same conditions and that of pure CNT samples were also measured and denoted as ZNC and CNT, respectively.

2.3 Characterization

The morphology and structure analyses were carried out on scanning electron microscopy (SEM, Hitachi SU-4800), transmitting electron microscopy (TEM, Fei Tecnai G2 F20 S-TWIN), X-ray diffraction (XRD, Shimadzu XRD-6000 diffractometer instrument), X-ray photoelectron spectroscopy (XPS, ESCA-LAB_250Xi X-ray photoelectron spectrometer), FTIR (Tensor 27 FTIR spectrometer) and Raman spectra (Laser Raman Spectroscopy, Renishaw RM1000). The N_2 sorption analysis was conducted with a Micromeritics specific area analyser (Micromeritics, 3Flex, SN#340) at 77 K applying the Brunauer-Emmett-Teller (BET) method for the specific surface area. The pore size distribution was obtained by using the density-functional-theory (DFT) model on the adsorption branch of the N_2 isotherm. Electrical conductivity was obtained from a four-point probe resistivity measurement system (RTS-8 Four Probes Tech).

2.4 Electrochemical evaluation

The as-prepared free-standing CNCF specimens were directly used as working electrode without any additives. Electrochemical experiments for individual electrodes were performed in a three-electrode configuration with Pt foil as counter electrode, Ag/AgCl as reference electrode and 6 M KOH as electrolyte. The cyclic voltammetry (CV), galvanostatic charge-discharge (GCD) and electrochemical impedance spectroscopy (EIS) data were recorded using a CHI660D electrochemical workstation (Chinstruments, China) at room temperature. For the Li-S battery test, the flexible S@CNCFs electrodes were prepared *via* a typical melt-infusion process. The S/CS₂ solution was first infiltrated into the CNCFs and then dried at $40 \text{ }^\circ\text{C}$. After heat treatment at $155 \text{ }^\circ\text{C}$ for 4 h under N_2 atmosphere, S@CNCFs with uniform sulfur distribution were obtained. The sulfur loading for each electrode was controlled at around 70 wt% by the addition of S/CS₂ solution.⁴² For the Li-S battery test, the flexible S@CNCF-5/1, S@CNCF-10/1 and S@CNCF-15/1 electrodes were prepared *via* a typical melt-infusion process, in which the sulfur loading for each electrode was controlled at around 70 wt%. The electrochemical measurements were carried out by using CR2025 coin cells, where the S@CNCF electrode served as cathodes. As for the aluminum-laminated, rectangular-shaped, soft-packed cell, the S@CNCF-10/1 electrode was cut into a $2 \times 3 \text{ cm}^2$ rectangular slice as cathode. Both coin and soft-packed cells used lithium foil as anode, Celgard 2400 membrane as separator and a solution of 1 M lithium bis(trifluoromethane sulfonyl)imide (LiTFSI) in a binary solvent of dimethoxyethane (DEM) and 1,3-dioxolane (DOL) (1 : 1 by volume), with 1 wt% lithium nitrate (LiNO_3) additive, as electrolyte. The GCD tests were performed using a LAND cyler (LAND, Wuhan China). The current and capacity were calculated based on the mass of the sulfur element. The EIS study was conducted using a CHI660D workstation with an

amplitude of 5 mV in the potential range of 1.8 V to 2.6 V (vs. Li⁺/Li).

3. Results and discussion

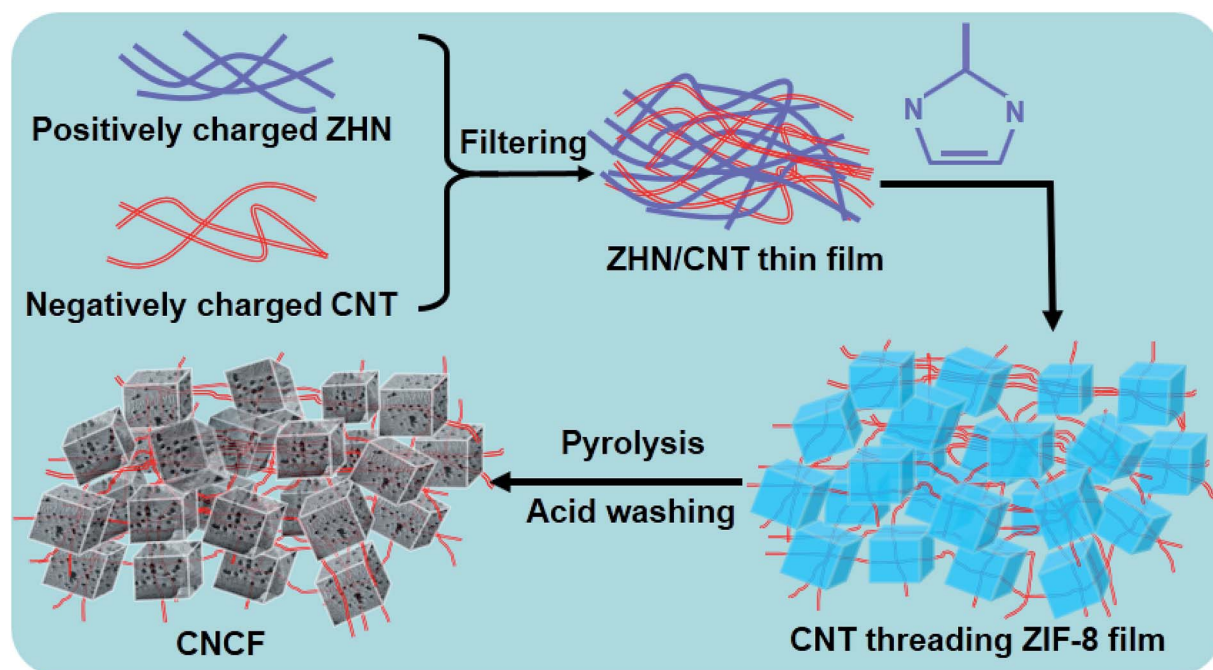
3.1 Physicochemical properties of CNCF

As shown in Scheme 1, the free-standing CNCF film was prepared *via* pyrolysis of the hybrid ZIF-8/CNT film. First, a ZHN/CNT hybrid film was obtained by filtering the homogeneous mixture of ZHN and CNT through vacuum filtration. Then, the ZIF-8/CNT thin film was prepared through *in situ* reaction by immersing ZHN/CNT into 2-methylimidazole (2-mIm) solution. Subsequently, after pyrolysis of ZIF-8/CNT film at 900 °C and washing with acid solution followed by abundant water, free-standing CNCF was obtained and used as electrode for supercapacitor and Li-S, respectively.

As shown in Fig. S1a,† the obtained ZHN/CNT thin film displays a well-ordered structure with a thickness of ~17 μm. After immersion in 2-mIm solution for 24 h, the thickness of the film increases to ~46 μm due to the successful formation of the crystalline ZIF-8 polyhedrons (Fig. 1a and b), as confirmed by the XRD pattern in Fig. S1b.† The peaks at 7.2°, 10.9°, 12.7°, 14.4°, 16.56°, 17.9°, 18.8°, 21.8°, 23.8°, 26.3°, 29.0°, and 30.2° are attributed to (011), (002), (112), (022), (013), (222), (123), (114), (233), (134), (044) and (334) crystal planes of ZIF-8, respectively.⁴³ Moreover, the CNT are partially threaded through the ZIF-8 crystals (Fig. 1c), contributing to the formation of interconnected carbon film. After pyrolysis and acid treatment, the ZIF-8/CNT precursor is transformed into a flexible three-dimensional (3D) interconnected carbon film, the thickness of which decreases to ~40 μm, and the carbon polyhedrons present a rough surface due to the decomposition of

functional groups during the pyrolysis (Fig. 1d–f). The thickness of CNCF-5/1 and CNCF-15/1 is ~40 μm as well (Fig. S1c and d†). The obtained CNCF in this work shows excellent flexibility and is capable of restoring its initial shape without any cracks after folding (Fig. S1e and f†). This could be ascribed to the CNT's interweavement in both longitudinal and transverse directions and to the porous features of the film, which help release stress and prevent damage of CNCF during bending. The ultimate tensile strengths of CNCF-5/1, 10/1 and 15/1 are 5.47 MPa, 4.66 MPa and 3.52 MPa with ultimate strains of about 2.67%, 2.15% and 1.53%, indicating that our films are mechanically robust and flexible (Fig. S2 and Movie S1†). In addition, based on the thickness and resistance, the electrical conductivities of CNCF-5/1, 10/1 and 15/1 were calculated as 1370 S m⁻¹, 1690 S m⁻¹ and 800 S m⁻¹, respectively.

The TEM images of CNCF-10/1 highlight CNT's penetration through the porous carbon (Fig. 1g). Magnification of the porous carbon (Fig. 1h) clearly shows the existence of abundant micro- and mesopores, demonstrating the nanoporous characteristic of the carbon material. Some of the pores are inherited from the porous ZIF-8 crystals, and others may come from the removal of Zn species during the acid treatment.²⁸ Moreover, the CNTs maintain their structures after the growth of ZIF-8 and pyrolysis at high temperature. The TEM images of CNCF-10/1@Zn are displayed in Fig. S3a.† The elemental mapping results of C, N, O and Zn (Fig. 1i and S3b†) confirm the uniform distribution of N atoms and the removal of Zn species after acid treatment. This unique structure composed of hierarchical porous carbon, heteroatom doping and CNT not only ensures wettability but also promotes charge transfer and improves ion diffusion efficiency.



Scheme 1 A schematic to fabrication of free-standing CNCF film.

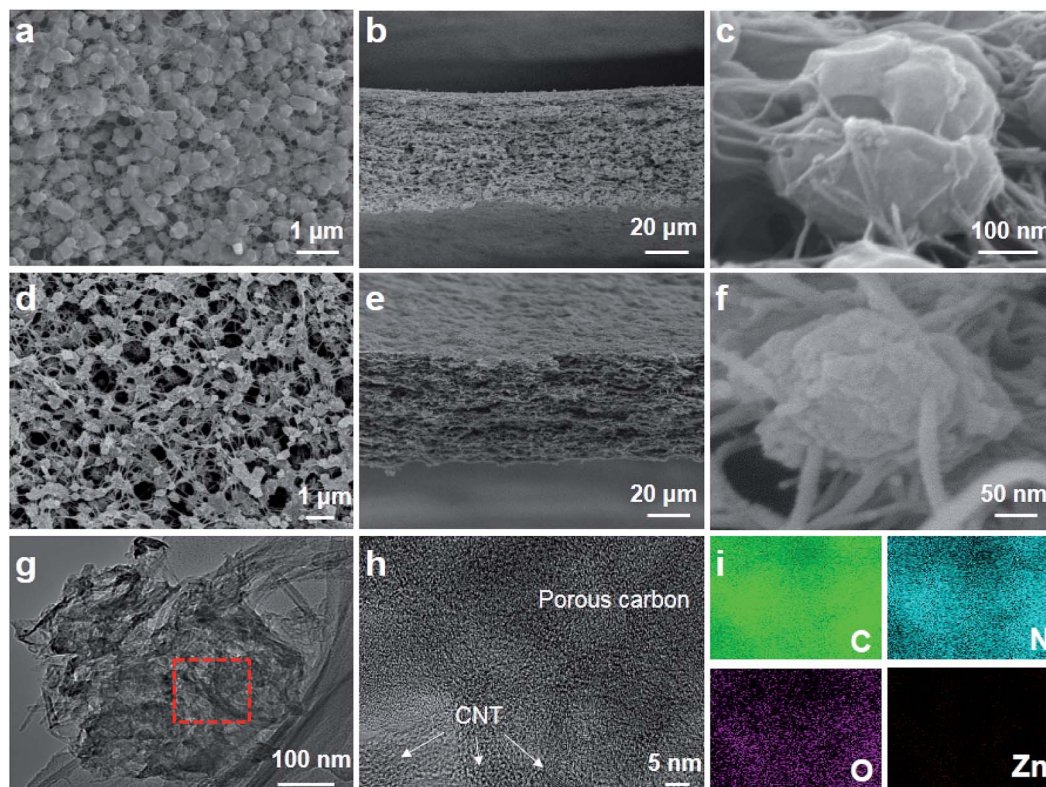


Fig. 1 SEM images of (a) surface and (b) cross section of 10/1 ZIF-8/CNT films; (d) surface and (e) cross section of CNCF-10/1 after pyrolysis; (c) and (f) are high-magnification SEM of (b) and (e), respectively; (g)–(i) are TEM, HRTEM images and mapping result of CNCF-10/1.

XPS was conducted to determine the chemical contents of CNCF-10/1@Zn and CNCF samples. The overview XPS spectra of all the samples (Fig. S4a[†]) show signals from C 1s, N 1s and O 1s, while the Zn 2p signals are only detected in CNCF-10/1@Zn.

This indicates the absence of Zn metals and the steady doping of N atoms in the carbon matrix, all of which agree with the TEM results. Fig. S4c[†] and 2a–c represent the detailed high-resolution XPS data of C 1s and N 1s peaks after

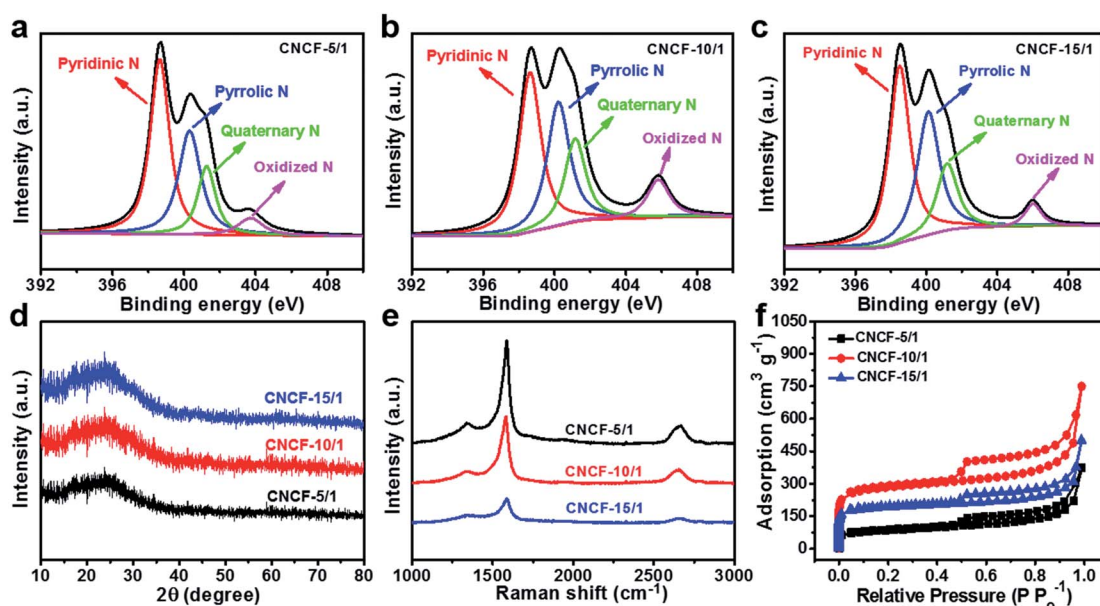


Fig. 2 (a)–(c) are the N 1s spectra of the samples, respectively; (d)–(f) represent the XRD, Raman, and N₂ adsorption/desorption isotherms of the samples, respectively.

deconvolution. For the C 1s spectra, the peaks at 284.4 eV correspond to the C–C bonds of sp^3 carbon, and the other peaks at 285.3 eV and 286.7 eV represent C–N (and C–O) and C=N (and C=O) functional groups, respectively.^{44,45}

A small peak at 290.7 eV can be assigned to π – π^* electronic transitions, confirming the presence of CNT.⁴⁶ The N 1s spectra can be mainly deconvoluted into four peaks, including pyridinic N (~ 398.6 eV), pyrrolic N (~ 400.1 eV), quaternary N (~ 401.2 eV) and oxidized N (~ 405.6 eV).⁴⁷ The atomic ratios according to the XPS measurements are summarized in Table 1; the nitrogen contents in the CNCF-5/1, 10/1 and 15/1 are 1.9 at%, 2.8 at% and 3.0 at%, respectively. Previous studies suggest that N atoms can enhance the conductivity of the carbon materials and provide additional pseudocapacitance together with structural defects by redox reactions.^{48,49} We further characterize the structure of the CNCF samples by XRD and Raman analysis. The XRD pattern (Fig. 2d) shows that all the samples present a prominent but obviously broadened peak at around 24° that can be assigned to the (002) plane, suggesting the amorphous state of the porous carbon. In the Raman spectra (Fig. 2e), apart from the disorder-induced D band (~ 1344 cm^{-1}) and in-plane vibrational G band (~ 1580 cm^{-1}), the samples also show a D* peak at ~ 2659 cm^{-1} , implying the existence of CNT.²⁸ It is generally accepted that the I_G/I_D value is a reflection of defects or disorder of the carbon lattice.⁵⁰ Hence, the lowest I_G/I_D value of CNCF-15/1 (Table 1) may originate from the increased structural defects induced by the higher heteroatom content.

Furthermore, the N_2 adsorption/desorption isotherm was measured to determine the detailed pore characteristics of the CNCF (Fig. 2f). The CNCF samples show a typical type IV adsorption/desorption isotherm with a sharp rise in the low-pressure and vertical tails at ~ 1.0 relative pressure, suggesting the coexistence of micro- and macropores. Additionally, the hysteresis loops indicate the existence of mesopores. Pore size distribution of the CNCF (Fig. S4d†) based on the density functional theory (DFT) further confirms the hierarchical porosity of the CNCF. The detailed pore structural characteristics are listed in Table 1. The CNCF-5/1 has the lowest S_{BET} value (467.6 m^2 g^{-1}) with the highest pore volume (0.85 cm^3 g^{-1}), which may be ascribed to its lowest porous carbon polyhedron content and excessive meso- and macropores formed by inter-CNT spaces. By comparison, the CNCF-10/1 shows a relatively

more compact structure with a S_{BET} value of 645.2 m^2 g^{-1} and pore volume of 0.46 cm^3 g^{-1} .

In view of the unique free-standing 3D interconnected conductive structure with high S_{BET} , hierarchical porosity and heteroatom doping, it is reasonable to expect the CNCF to possess exceptional conductivity, short ion diffusion path and low diffusion resistance, making it a promising electrode for the supercapacitor and Li–S battery, respectively.

3.2 Electrochemical behavior of CNCF for supercapacitor electrode

Encouraged by the hierarchical porous structure of the CNCFs, a three-electrode configuration was carried out to investigate their supercapacitive performance in 6 M KOH aqueous electrolyte. We firstly conducted a CV test for all the samples at 100 mV s^{-1} . As shown in Fig. 3a, the curves of CNCF-5/1, 10/1 and 15/1 show rectangle-like shapes with a few humps caused by pseudocapacitive processes. The electrical double-layer capacitance (EDLC) and the pseudocapacitance can be separated and calculated from the CV curve, respectively (Fig. S5a and b†).^{51,52} The CNCF-10/1 possesses the largest EDLC, while the CNCF-15/1 has the largest pseudocapacitance, implying the contribution of S_{BET} and dopants to the increased charge storage capability.

Since it is well recognized that the GCD test is more reliable than the CV test for determining the specific capacitance,⁵³ here the GCD profiles were carried out at different current densities. The GCD profiles of the CNCFs, ZNC and CNT at 2 A g^{-1} and the profiles for CNCF-10/1 from 20 A g^{-1} to 400 A g^{-1} are shown in Fig. S5c† and 3b, respectively. All these curves are symmetric, and the shapes are well maintained even at a high current density of 400 A g^{-1} , suggesting the robust electrochemical response and fast-ion adsorption–desorption at the electrode/electrolyte interfaces. The gravimetric capacitance as a function of current density was calculated (based on eqn (1) in ESI†) and is summarized in Fig. S5d.† The specific capacitance was calculated for CNCF-5/1, CNCF-10/1 and CNCF-15/1 to be 243, 340 and 270 F g^{-1} at 2 A g^{-1} , respectively, while the capacitance values of ZNC and CNT were 180 and 70 F g^{-1} under the same current density. This means that the large capacitance of the CNCFs primarily comes from the ZIF-8 derived porous carbon, with minor contribution from the CNT. On the other hand, the

Table 1 Composition, pore characteristics, electrical conductivity and Raman results of the samples

| | XPS ^a /at% | | | S_{BET} ^b / m^2 g^{-1} | S_{micro} ^c / m^2 g^{-1} | V_t ^d / cm^3 g^{-1} | D_{ave} ^e /nm | I_G/I_D ^f | Conductivity ^g /S m^{-1} |
|-----------|-----------------------|-----|-----|---|---|--------------------------------------|----------------------------|------------------------|---------------------------------------|
| | C | N | O | | | | | | |
| CNCF-5/1 | 93.4 | 2.7 | 4.0 | 467.6 | 178.5 | 0.85 | 7.30 | 1.90 | 1583 |
| CNCF-10/1 | 91.2 | 3.9 | 4.8 | 645.2 | 406.9 | 0.46 | 2.85 | 1.79 | 1538 |
| CNCF-15/1 | 90.5 | 4.8 | 4.7 | 599.8 | 425.4 | 0.43 | 2.86 | 1.16 | 793 |

^a Atomic percentage of elements obtained from XPS analysis. ^b Specific surface area was calculated by Brunauer–Emmett–Teller (BET) equation. ^c Specific surface area of micropores was calculated by t -plot method. ^d The total pore volume was determined from the amount of nitrogen adsorbed at a relative pressure of 0.99. ^e The average pore size was obtained from the equation: $D_{ave} = 4 \times V_t/S_{BET}$. ^f I_G/I_D is the integral intensity of the G and D bands. ^g Conductivity was tested by four-probe conductivity test.

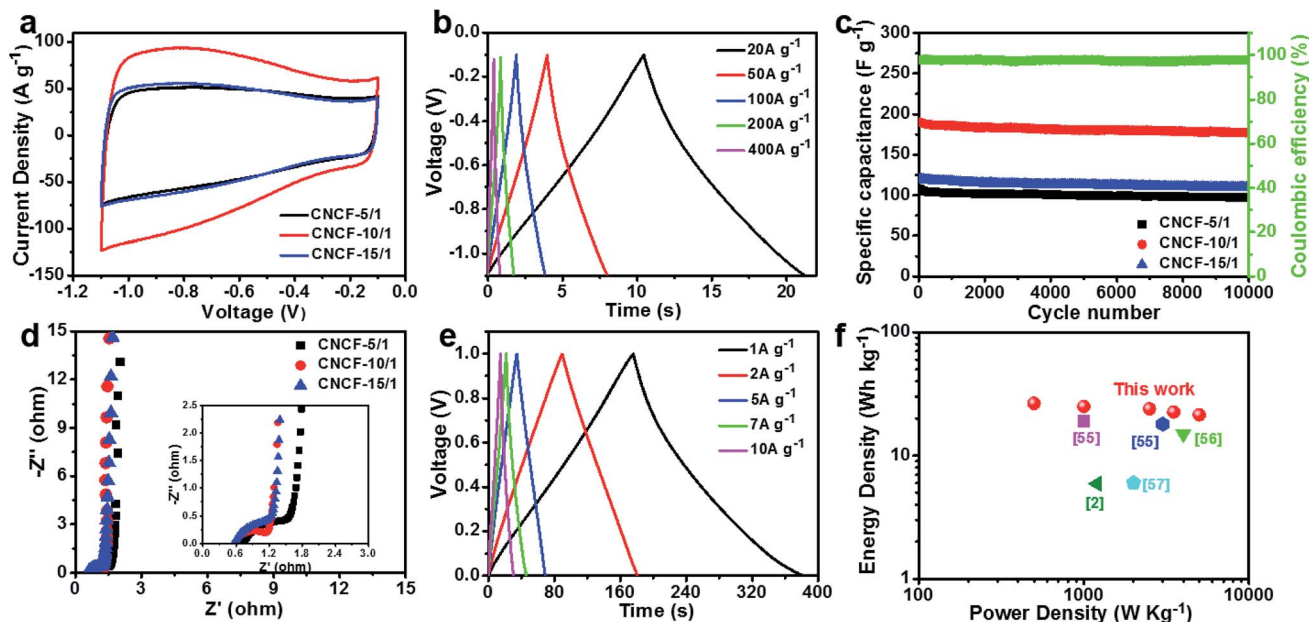


Fig. 3 (a) CV curves of the samples at 100 mV s^{-1} ; (b) GCD curves of CNCF-10/1 at different current densities; (c) and (d) are the cycling performance and EIS spectra of the samples; (e) GCD curves of the CNCF-10/1-based symmetric supercapacitor cell; (f) the Ragone plots and performance comparison of the as-prepared symmetric cell vs. previously reported carbon symmetric supercapacitors in aqueous electrolyte.

capacitance decay rates of CNCF-5/1, CNCF-10/1 and CNCF-15/1 were 27% (152 F g^{-1} to 111 F g^{-1}), 20% (254 F g^{-1} to 201 F g^{-1}) and 24% (156 F g^{-1} to 118 F g^{-1}) as the current density increased from 5 A g^{-1} to 50 A g^{-1} , confirming the impressive capacitive behavior and rate performance of CNCF-10/1. Moreover, the CNCF-10/1 retained 43% of its initial specific capacitance when the current density increased to 400 A g^{-1} . Though some MOF-derived porous carbons, ZIF-8 included, have been used as electrode material for supercapacitors, their electrochemical performance is inferior to CNCF-10/1 (Table S1[†]). Besides, our result is also higher than those of other flexible carbon electrodes in aqueous electrolyte (Table S2[†]). The outstanding performance of CNCF is due to the high electrical conductivity, sufficient physical contact points and continuous electrolyte ion diffusion pathways throughout the electrode, generated from the rich cross-linked CNT/carbon-polyhedron network.

We also explored the effect of film thickness on the capacitive behaviour. CNCF-10/1 with different thicknesses ($40 \mu\text{m}$, $60 \mu\text{m}$ and $80 \mu\text{m}$) were prepared, and their electrochemical performance at 2 A g^{-1} was measured (Fig. S5e[†]). Obviously, $40 \mu\text{m}$ was the optimal thickness for CNCF-10/1, as $60 \mu\text{m}$ and $80 \mu\text{m}$ films had shorter discharging time than $40 \mu\text{m}$. The smaller capacitance of $60 \mu\text{m}$ and $80 \mu\text{m}$ CNCF-10/1 can be attributed to the higher inner ionic diffusion resistance caused by the increased thickness, as confirmed by the EIS results (Fig. S5f[†]).

The long-term cycling tests of the samples were conducted by repeating the GCD test at a high current density of 20 A g^{-1} for 10 000 cycles (Fig. 3c). The CNCF-10/1 shows a coulombic efficiency of up to 97.7%, higher than that of CNCF-5/1 (91.1%) and CNCF-15/1 (91.4%). Fig. 3d shows the Nyquist plots of CNCF-5/1 to CNCF-15/1 electrodes. The diameter of the semicircle from

the high- to mid-frequency region indicates the charge transfer resistance (R_{ct}). Obviously, CNCF-5/1 displayed the largest R_{ct} , while CNCF-10/1 displayed the smallest, indicating the lowest charge transfer resistance and highest ionic conductivity of the CNCF-10/1 electrode. In addition, judging from the intersection of the real axis, which reflects the equivalent series resistance (R_s), CNCF-10/1 and CNCF-15/1 present similar R_s , while CNCF-5/1 shows the largest. The lowest equivalent internal resistance, coupled with the highest electrical conductivity, proper N-doping content, and the highest BET surface area result in the best electrochemical performance of CNCF-10/1.

We also assembled a symmetric supercapacitor cell based on CNCF-10/1 to further explore its application potential. The GCD curves show linear and near-triangular shapes within the voltage window of 0–1.0 V (Fig. 3e), suggesting a small resistance and ideal capacitive behavior. The specific capacitance was 191.2 F g^{-1} (calculated from eqn (1) in ESI[†]) at 1 A g^{-1} , and 80% of the initial capacitance was retained at 10 A g^{-1} , demonstrating the excellent rate capability of CNCF-10/1. The energy density and power density were also calculated (based on eqn (2) and (3) in ESI[†]) and are shown in Fig. 3f. The Ragone plot of the CNCF-10/1//CNCF-10/1 symmetric supercapacitor shows a maximum energy density of 26.6 W h kg^{-1} and remains at 21.1 W h kg^{-1} with a power density of 5000 W kg^{-1} —superior to those of recently reported heteroatom-doped, carbon-based aqueous symmetric supercapacitors.^{2,54–57}

3.3 Electrochemical performance of CNCF for Li-S battery cathode

As for the Li-S battery, the CNCF with high S_{BET} and outstanding conductive networks can serve as effective host for sulfur species. In addition, the functional N species show great

capability for chemisorption of sulfur and polysulfides, which not only provides more reactive sites but also promotes polysulfide fixation for improved Li-S battery.^{58,59} Hence, the free-standing CNCFs are also considered as an excellent choice for the Li-S battery.

Sulfur electrode based on the CNCF (S@CNCF) was prepared *via* a typical melt-infusion process. The sulfur content in the S@CNCF electrode was controlled at $\sim 70\%$, as confirmed by the TGA analysis (Fig. S6†). As shown in Fig. S7a,† the S@CNCF-10/1 electrode presents similar thickness ($\sim 40\ \mu\text{m}$) and lamellate structure to that of the pristine CNCF-10/1, indicating the good structural integrity of the CNCF during the sulfur loading process. The TEM and elemental mapping results (Fig. S7c and d†) reveal the good dispersion of sulfur in the carbon matrix, matching well with the XRD result of S@CNCF-10/1 (Fig. S7b†).⁶⁰ The ultimate tensile strength of the S@CNCF-10/1 is maintained at 2.46 MPa with a strain around 1.26%, implying that our sulfur electrode still retains mechanical flexibility.

The electrochemical performance of S@CNCF electrodes as cathode in Li-S battery with a sulfur loading of $3\ \text{mg}\ \text{cm}^{-2}$ is shown in Fig. 4. The galvanostatic charge-discharge test (Fig. 4a) of S@CNCF-5/1, 10/1 and 15/1 shows typical two-platform voltage curves in the discharge process, corresponding to the electrochemical reduction of S_8 to soluble long-chain

polysulfides Li_2S_x ($x = 4-8$) at 2.3 V and, subsequently, to short-order insoluble $\text{Li}_2\text{S}_2/\text{Li}_2\text{S}$ at 2.1 V, respectively.⁶¹⁻⁶⁴ Noticeably, the S@CNCF-10/1 delivers a high initial capacity of $1258.8\ \text{mA}\ \text{h}\ \text{g}^{-1}$, much higher than those of S@CNCF-5/1 and S@CNCF-15/1. Fig. 4b compares the cycling performance of S@CNCF-5/1, 10/1 and 15/1 at a current density of C/5. The discharge capacity of S@CNCF-5/1 and 15/1 decreased to $763.3\ \text{mA}\ \text{h}\ \text{g}^{-1}$ and $890.5\ \text{mA}\ \text{h}\ \text{g}^{-1}$, with the low capacity retention of 68.6% and 48.8% after 100 cycles, respectively. In contrast, the S@CNCF-10/1 retains a discharge capacity of $1104.1\ \text{mA}\ \text{h}\ \text{g}^{-1}$ after 100 cycles, corresponding to a capacity retention of 87.0%—higher than that of 5/1 and 15/1. The outstanding cyclability of S@CNCF-10/1 can be explained by the EIS result (Fig. 4c). S@CNCF-10/1 has the smallest R_{ct} and R_w , indicating an accelerated charge transfer process in the highly conductive porous carbon. Thus, it can be suggested that the CNCF-10/1 is the best sulfur host among the samples.

Besides, sulfur electrodes based on CNT (S@CNT) and ZNC (S@ZNC) were prepared *via* the conventional slurry-coating method. The cycling performance of S@CNT and S@ZNC was also measured at the rate of C/5 with a sulfur loading of $3\ \text{mg}\ \text{cm}^{-2}$ (Fig. S8a†). In contrast, the S@CNT and S@ZNC electrodes show much lower initial capacity (947.1 and $1030.7\ \text{mA}\ \text{h}\ \text{g}^{-1}$, respectively) as well as inferior capacity retention (61% and 67%, respectively) than those of the S@CNCF-10/1 after 50

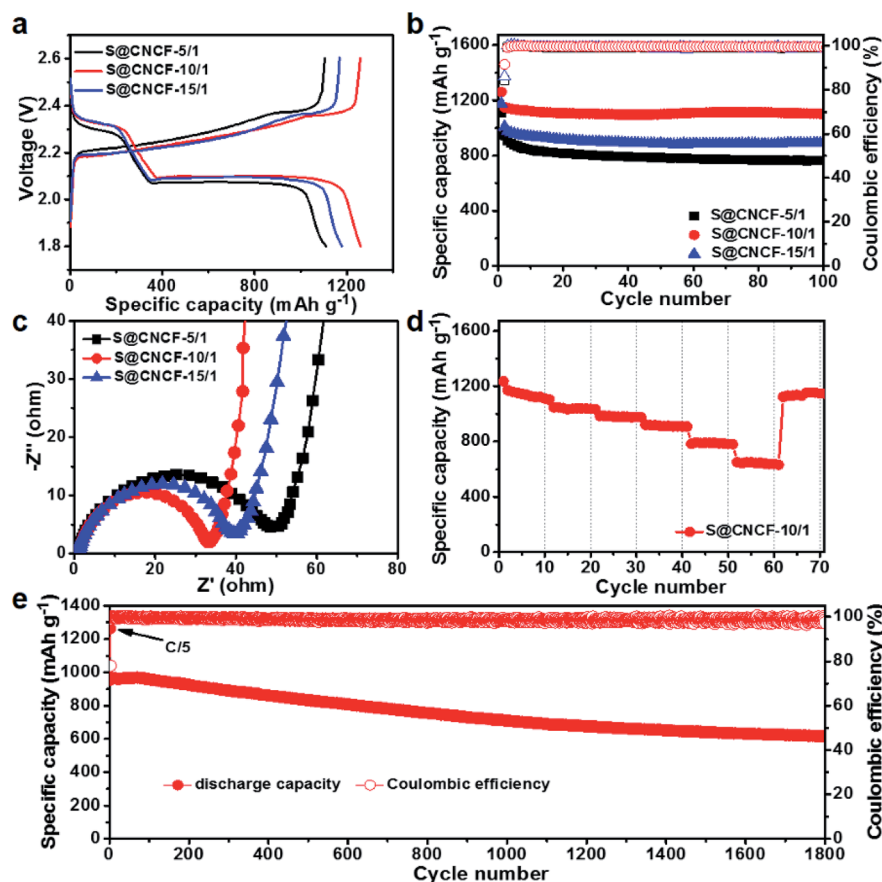


Fig. 4 (a) The first charge-discharge curves and (b) cycling performance of S@CNCF-5/1, 10/1 and 15/1 at C/5; (c) EIS tests of the samples; (d) rate performance of S@CNCF-10/1 at various current densities from 0.2C to 10C; (e) long-term cycling performance of S@CNCF-10/1 at 1C.

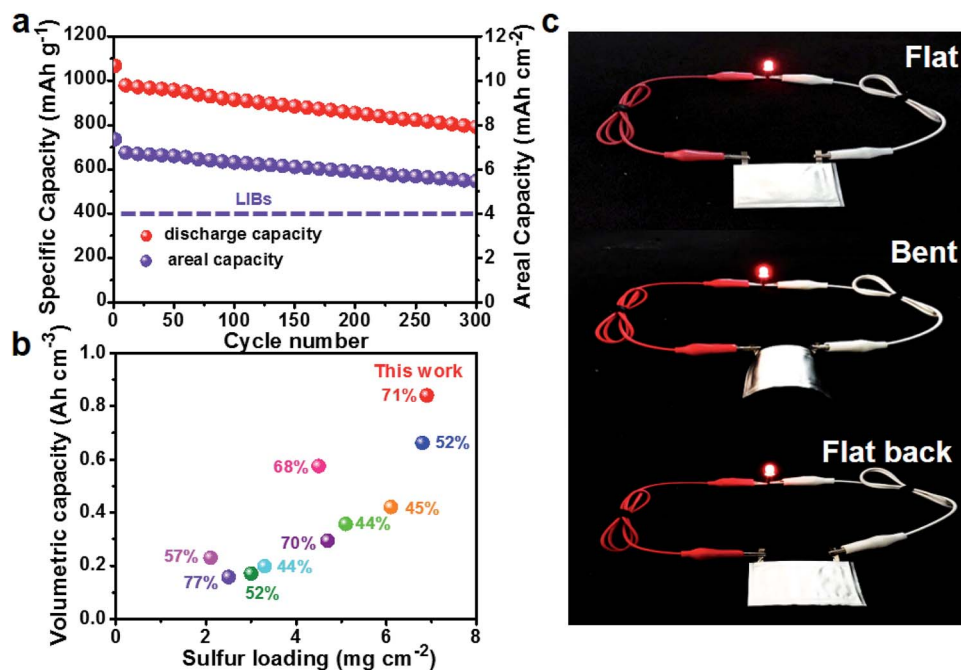


Fig. 5 (a) Cycling performance of S@CNCF-10/1 with high sulfur loading at C/5; (b) comparisons of volumetric capacity and sulfur weight content of the S@CNCF-10/1 with those of other self-standing sulfur electrodes; (c) photographs of a soft-package Li-S battery lighting a red LED device under flat and bent states.

cycles. The excellent performance of S@CNCF-10/1 is due to its superior structural integrity originating from the synergistic effect of CNT and ZIF-8-derived porous carbon polyhedrons with small electrochemical impedance (Fig. S8b†).

The multi-rate test of S@CNCF-10/1 was further performed to study its rate capability. In Fig. 4d, the S@CNCF-10/1 obtains a capacity of 1235 mA h g⁻¹, 986 mA h g⁻¹, and 782 mA h g⁻¹ at current densities of C/5, 1C and 5C, respectively. As the current density increases to 10C, a high capacity of 652 mA h g⁻¹ is still restored. Furthermore, when the current density is abruptly reduced back to C/5, the capacity is recovered to 1147 mA h g⁻¹, demonstrating the electrode's robust electrochemical kinetics and excellent rate performance. Moreover, the S@CNCF-10/1 exhibits considerable long-term stability at the high current rate of 1C. As shown in Fig. 4e, a discharge capacity of 973 mA h g⁻¹ is achieved after an initial activation process at C/5. The capacity remains at 926 mA h g⁻¹ after 200 cycles, indicative of only 4.8% capacity loss, and 807 mA h g⁻¹ after 600 cycles, presenting a capacity loss of 11.1%. Even when the cycle life is extended to 1800 cycles, the capacity still remains at 614 mA h g⁻¹, corresponding to a capacity retention of 64.1% and an overall capacity decay rate as low as 0.02%/cycle. The excellent cycling stability achieved in this work is superior to that of other nitrogen-doped carbon materials (Table S3†). These results powerfully demonstrate the CNCF's high efficiency in confining/absorbing polysulfides, restraining the shuttle phenomenon, and its superb structural integrity during the long-term charge-discharge process.

Since high sulfur loading is crucial to satisfy the high energy density demand for practical application, the sulfur loading was raised to 6.9 mg cm⁻² (~71 wt%) to explore the practical

potential of S@CNCF. The cycling stability of S@CNCF-10/1 at C/5 with a sulfur loading of 6.9 mg cm⁻² is shown in Fig. 5a. The electrode exhibits an initial discharge capacity of 1067 mA h g⁻¹ and remains above 790 mA h g⁻¹ after 300 cycles. Moreover, the electrode obtains an initial areal capacity of 7.3 mA h cm⁻² and stabilizes at 5.5 mA h cm⁻² even after 300 cycles, exceeding that of commercial Li-ion battery (around 4.0 mA h cm⁻²). More importantly, the initial volumetric capacity reaches 0.94 A h cm⁻³ and still remains at 0.84 A h cm⁻³ at the 50th cycle, which is much higher than that of other free-standing carbon-based sulfur cathodes reported previously (Fig. 5b and Table S4†). Aiming to verify the flexibility of the electrode, we fabricated a soft-package Li-S cell based on S@CNCF-10/1. This soft-package Li-S cell is able to light up a red LED when it is flat or bent, implying excellent flexibility and stability, as shown in Fig. 5c.

The superior electrochemical performance of the CNCF for Li-S battery can be attributed to the structural advantages. First, the ZIF-8-derived porous carbon provides the electrode with a large surface area that not only increases the contact area for electrolyte ions but also helps the uniform distribution of sulfur and allows high sulfur loading for improved energy density. Second, the nitrogen dopants can strengthen the immobilization of the soluble polysulfides by additional chemisorption. Third, the CNT threads the electrode into a flexible and conductive film, effectively improving the electrical conductivity and suppressing the volume expansion during the charge-discharge process. Finally, the interconnected hierarchical porous structure offers smooth and continuous electrical pathways for ion diffusion.

4. Conclusions

In conclusion, we have prepared free-standing, CNT-threaded nitrogen-doped porous carbon film (CNCF) through simple pyrolysis of CNT-threaded ZIF-8 polyhedron film for application in binder-free supercapacitor and Li-S battery. When applied as supercapacitor electrode, the as-prepared CNCF-10/1 displays a high specific capacitance of 340 F g^{-1} at 2 A g^{-1} and good cyclic stability at 20 A g^{-1} . The CNCF-10/1//CNCF-10/1 symmetric supercapacitor cell shows a high energy density of 21.1 W h kg^{-1} with a power density of 5000 W kg^{-1} . When used as sulfur cathode, the S@CNCF-10/1 electrode exhibits an extraordinary cyclability of up to 1800 cycles with an ultralow capacity decay rate of $0.02\%/cycle$ at 1C. It also obtains high energy density at high sulfur loading (6.9 mg cm^{-2}), e.g. an initial areal capacity of 7.3 mA h cm^{-2} and a volumetric capacity of 0.94 A h cm^{-3} . This work opens up a promising approach to the design of free-standing and flexible nitrogen-doped porous carbon thin film for binder-free, high-performance supercapacitor and Li-S battery.

Acknowledgements

This work was supported by the National Basic Research Program of China 973 Program (2015CB655302), National Key Research and Development Program (2016YFA0200204), Key program of National Natural Science and Foundation (NSFC 51632008), and the National Natural Science Foundations of China (NSFC 21671171).

Notes and references

- H. J. Peng, J. Q. Huang, M. Q. Zhao, Q. Zhang, X. B. Cheng, X. Y. Liu, W. Z. Qian and F. Wei, *Adv. Funct. Mater.*, 2014, **24**, 2772–2781.
- Y. Cheng, L. Huang, X. Xiao, B. Yao, L. Yuan, T. Li, Z. Hu, B. Wang, J. Wan and J. Zhou, *Nano Energy*, 2015, **15**, 66–74.
- J. Z. Guo, X. L. Wu, F. Wan, J. Wang, X. H. Zhang and R. S. Wang, *Chem.-Eur. J.*, 2015, **21**, 17371–17378.
- J. Cheng, Y. Pan, J. Zhu, Z. Li, J. Pan and Z. Ma, *J. Power Sources*, 2014, **257**, 192–197.
- Z. Ma, H. Wu, Y. Wang, Y. Pan and C. Lu, *Int. J. Plast.*, 2017, **88**, 188–203.
- C. Wang, Z. Ma, Y. Wang and C. Lu, *J. Electrochem. Soc.*, 2016, **163**, A1157–A1163.
- H. J. Peng, T. Z. Hou, Q. Zhang, J. Q. Huang, X. B. Cheng, M. Q. Guo, Z. Yuan, L. He and F. Wei, *Adv. Mater. Interfaces*, 2014, **1**, 1400227.
- Y. Zhao, W. Wu, J. Li, Z. Xu and L. Guan, *Adv. Mater.*, 2014, **26**, 5113–5118.
- L. Jiang, L. Sheng, C. Long and Z. Fan, *Nano Energy*, 2015, **11**, 471–480.
- S. Xin, Y. G. Guo and L. J. Wan, *Acc. Chem. Res.*, 2012, **45**, 1759–1769.
- X. Gao, Y. Wang, Z. Ma, W. Jiang, Y. Zou and C. Lu, *J. Mater. Sci.*, 2016, **51**, 5139–5145.
- Z. Y. Yu, L. F. Chen, L. T. Song, Y. W. Zhu, H. X. Ji and S. H. Yu, *Nano Energy*, 2015, **15**, 235–243.
- M. Ghaffari, Y. Zhou, H. Xu, M. Lin, T. Y. Kim, R. S. Ruoff and Q. M. Zhang, *Adv. Mater.*, 2013, **25**, 4879–4885.
- H. Wang, H. Yi, C. Zhu, X. Wang and H. J. Fan, *Nano Energy*, 2015, **13**, 658–669.
- J. X. Zhang, Z. S. Ma, J. J. Cheng, Y. Wang, C. Wu, Y. Pan and C. Lu, *J. Electroanal. Chem.*, 2015, **738**, 184–187.
- J. J. Cheng, Y. Pan, J. A. Pan, H. J. Song and Z. S. Ma, *RSC Adv.*, 2015, **5**, 68–74.
- C. Long, L. Jiang, X. Wu, Y. Jiang, D. Yang, C. Wang, T. Wei and Z. Fan, *Carbon*, 2015, **93**, 412–420.
- L. Qie, W. Chen, H. Xu, X. Xiong, Y. Jiang, F. Zou, X. Hu, Y. Xin, Z. Zhang and Y. Huang, *Energy Environ. Sci.*, 2013, **6**, 2497.
- Z. S. Wu, A. Winter, L. Chen, Y. Sun, A. Turchanin, X. Feng and K. Mullen, *Adv. Mater.*, 2012, **24**, 5130–5135.
- H. P. Cong, X. C. Ren, P. Wang and S. H. Yu, *Energy Environ. Sci.*, 2013, **6**, 1185.
- L. Liu, Y. Yu, C. Yan, K. Li and Z. Zheng, *Nat. Commun.*, 2015, **6**, 7260.
- L. Kou, T. Huang, B. Zheng, Y. Han, X. Zhao, K. Gopalsamy, H. Sun and C. Gao, *Nat. Commun.*, 2014, **5**, 3754.
- K. Xie and B. Wei, *Adv. Mater.*, 2014, **26**, 3592–3617.
- H. Zhang, K. Wang, X. Zhang, H. Lin, X. Sun, C. Li and Y. Ma, *J. Mater. Chem. A*, 2015, **3**, 11277–11286.
- K. S. Novoselov, V. I. Fal'ko, L. Colombo, P. R. Gellert, M. G. Schwab and K. Kim, *Nature*, 2012, **490**, 192–200.
- H. Chang and H. Wu, *Energy Environ. Sci.*, 2013, **6**, 3483.
- Y. Sun, Q. Wu and G. Shi, *Energy Environ. Sci.*, 2011, **4**, 1113.
- Y. Fang, B. Luo, Y. Jia, X. Li, B. Wang, Q. Song, F. Kang and L. Zhi, *Adv. Mater.*, 2012, **24**, 6348–6355.
- C. Uthaisar and V. Barone, *Nano Lett.*, 2010, **10**, 2838–2842.
- P. Zhang, F. Sun, Z. Xiang, Z. Shen, J. Yun and D. Cao, *Energy Environ. Sci.*, 2014, **7**, 442–450.
- B. Liu, H. Shioyama, T. Akita and Q. Xu, *J. Am. Chem. Soc.*, 2008, **130**, 5390–5391.
- R. R. Salunkhe, Y. Kamachi, N. L. Torad, S. M. Hwang, Z. Sun, S. X. Dou, J. H. Kim and Y. Yamauchi, *J. Mater. Chem. A*, 2014, **2**, 19848–19854.
- Y. Gao, J. Wu, W. Zhang, Y. Tan, J. Gao, J. Zhao and B. Tang, *Solid-State Electron.*, 2014, **18**, 3203–3207.
- M. Jiang, X. Cao, D. Zhu, Y. Duan and J. Zhang, *Electrochim. Acta*, 2016, **196**, 699–707.
- F. Bai, Y. Xia, B. Chen, H. Su and Y. Zhu, *Carbon*, 2014, **79**, 213–226.
- K. Lu, J. Xu, J. Zhang, B. Song and H. Ma, *ACS Appl. Mater. Interfaces*, 2016, **8**, 17402–17408.
- G. Huang, F. Zhang, X. Du, Y. Qin, D. Yin and L. Wang, *ACS Nano*, 2014, **9**, 1592–1599.
- Y. Zhang, B. Lin, J. Wang, J. Tian, Y. Sun, X. Zhang and H. Yang, *J. Mater. Chem. A*, 2016, **4**, 10282–10293.
- F. Jin, S. Xiao, L. Lu and Y. Wang, *Nano Lett.*, 2016, **16**, 440–447.
- M. Q. Zhao, X. F. Liu, Q. Zhang, G. Li, J. Q. Huang, W. Zhu and F. Wei, *ACS Nano*, 2012, **6**, 10759–10769.

- 41 Y. Liu, H. W. Huang and X. S. Peng, *Electrochim. Acta*, 2013, **104**, 289–294.
- 42 C. Wang, H. Zhang, C. Feng, S. Gao, N. Shang and Z. Wang, *Catal. Commun.*, 2015, **72**, 29–32.
- 43 Y. Mao, G. Li, Y. Guo, Z. Li, C. Liang, X. Peng and Z. Lin, *Nat. Commun.*, 2017, **8**, 14628.
- 44 R. R. Salunkhe, J. Tang, Y. Kamachi, T. Nakat, J. H. Kim and Y. Yamauchi, *ACS Nano*, 2015, **6**, 6288–6296.
- 45 J. Chen, J. Xu, S. Zhou, N. Zhao and C. P. Wong, *Nano Energy*, 2016, **25**, 193–202.
- 46 T. I. T. Okpalugo, P. Papakonstantinou, H. Murphy, J. M. Laughlin and N. M. D. Brown, *Carbon*, 2005, **43**, 2951–2959.
- 47 J. Cai, C. Wu, Y. Zhu, K. Zhang and P. K. Shen, *J. Power Sources*, 2017, **341**, 165–174.
- 48 J. Wang, L. Shen, P. N. Xie, X. Yun, Y. I. Xu, H. Dou and X. Zhang, *J. Mater. Chem. A*, 2015, **3**, 2853–2860.
- 49 J. Zhou, J. Lian, L. Hou, J. Zhang, H. Gou, M. Xia, Y. Zhao, T. A. Strobel, L. Tao and F. Gao, *Nat. Commun.*, 2015, **6**, 8503.
- 50 L. F. Chen, Z. H. Huang, H. W. Liang, W. T. Yao, Z. Y. Yu and S. H. Yu, *Energy Environ. Sci.*, 2013, **6**, 3331.
- 51 Z. Lin, Y. Liu, Y. Yao, O. J. Hildreth, Z. Li, K. Moon and C. P. Wong, *J. Phys. Chem. C*, 2011, **115**, 7120–7125.
- 52 Y. Hu, H. Liu, Q. Ke and J. Wang, *J. Mater. Chem. A*, 2014, **2**, 11753.
- 53 M. D. Stoller and R. S. Ruoff, *Energy Environ. Sci.*, 2010, **3**, 1294.
- 54 Y. Q. Zhao, M. Lu, P. Y. Tao, Y. J. Zhang, X. T. Gong, Z. Yang, G. Q. Zhang and H. L. Li, *J. Power Sources*, 2016, **307**, 391–400.
- 55 Y. Li, G. Wang, T. Wei, Z. Fan and P. Yan, *Nano Energy*, 2016, **19**, 165–175.
- 56 X. Wei, S. Wan and S. Gao, *Nano Energy*, 2016, **28**, 206–215.
- 57 F. Sun, J. Gao, X. Pi, L. Wang, Y. Yang, Z. Qu and S. Wu, *J. Power Sources*, 2017, **337**, 189–196.
- 58 J. Qu, S. Lv, X. Peng, S. Tian, J. Wang and F. Gao, *J. Alloys Compd.*, 2016, **671**, 17–23.
- 59 H. Wang, K. Huang, P. Wang and J. Zhong, *J. Alloys Compd.*, 2017, **691**, 613–618.
- 60 J. J. Cheng, J. T. Zhu, Y. Pan, Z. S. Ma, H. J. Song, J. A. Pan, Z. Z. Li and C. Lu, *ECS Electrochem. Lett.*, 2014, **4**, A19–A21.
- 61 F. Pei, T. An, J. Zang, X. Zhao, X. Fang, M. Zheng, Q. Dong and N. Zheng, *Adv. Energy Mater.*, 2016, **6**, 1502539.
- 62 J. Cheng, Y. Pan, J. Zhu, Z. Li, J. Pan and Z. Ma, *J. Power Sources*, 2014, **257**, 192–197.
- 63 X. Meng, D. J. Comstock, T. T. Fister and J. W. Elam, *ACS Nano*, 2014, **8**, 10963–10972.
- 64 Z. Z. Li, Y. Pana, J. J. Cheng, J. A. Pan, L. Li, C. Wu, P. Gao and Z. S. Ma, *J. Polym. Mater.*, 2015, **32**, 237–246.